Article:
Zhang, G., Ingham, D., Ma, L. et al. (2022) Modelling of 3D liquid dispersion in a rotating packed bed using an Eulerian porous medium approach. Chemical Engineering Science, 250. 117393. ISSN: 0009-2509

https://doi.org/10.1016/j.ces.2021.117393

Modelling of 3D liquid dispersion in a rotating packed bed using an Eulerian porous medium approach

Guojun Zhang, Derek Ingham, Lin Ma*, Mohamed Pourkashanian

Energy 2050, Mechanical Engineering, Faculty of Engineering, University of Sheffield, Sheffield S10 2TN, UK

Abstract: Liquid dispersion is very important for the modelling of liquid flow in a rotating packed bed (RPB) when an Eulerian porous medium approach is employed. For investigating the effect of the liquid dispersion in a practical RPB, a 3D Eulerian porous medium model has been established coupled with the appropriate interfacial, drag and dispersion forces formulations. The sensitivity of the parameters employed in these formulations has been thoroughly analyzed. New forms of the porous resistance model and the effective interfacial area correlation have been developed for the non-uniform two-phase flows. The simulation results show that the effect of the capillary pressure and mechanical dispersion forces on the liquid flow distribution and holdup in the RPB is clear and important. In addition, the effects of the dispersion force on the liquid holdup under different design and operational parameters have been thoroughly analyzed and it is found that the effect of the dispersion forces on the liquid holdup is almost the same for different nozzle widths and the porosities of the packing investigated. The investigation demonstrates that utilizing the Eulerian method can substantially reduce the simulation time and efforts when compared to the pore resolved method, such as the Volume of Fluid method without loss in accuracy. This provides a feasible approach to simulate RPBs in full 3D and for RPB technology scaling up and optimizations.

Keywords: rotating packed bed, Eulerian method, liquid dispersion, porous media, 3D modelling

Highlights：

- A novel 3D Eulerian porous medium model is developed for the gas-liquid flow in a RPB.
- The sensitivity of the capillary pressure and mechanical dispersion models is analyzed.
- The effect of liquid dispersion under different design and operational parameters are obtained.
- The established model paves the way for simulating a 3D full scale RPB effectively and accurately.

Nomenclatures

a_S	specific area of the packing materials, $m^2 \cdot m^{-3}$	U_l	characteristic flow rate per unit area (=0.0106 $m \cdot s^{-1}$), $m \cdot s^{-1}$
a_S'	specific area of the wet wires, $m^2 \cdot m^{-3}$	$\vec{v}_{D,i}$	drift velocity of phase *i*, $m \cdot s^{-1}$
A_{GL}	effective interfacial area, m^{-1}	v_e	effective velocity relative to the rotating packing, $m \cdot s^{-1}$
d_w	diameter of the wire mesh, m	$\vec{v}_i$	velocity of phase *i* relative to the rotating packing, $m \cdot s^{-1}$
d_w'	wire and liquid film diameter, m	$\vec{v}_i'$	superficial velocity of phase *i* relative to the rotating packing, $m \cdot s^{-1}$
d_{min}	characteristic diameter, m	V	volume, m^3
D_h	hydraulic diameter, m	$\mathcal{X}^+$	dimensionless channel length
f_l	fanning friction factor for developing laminar flow	Z	axial coordinate
f_e	ratio of wetted packing or ratio of interfacial area to the total packing surface area	*Greek*	
f_t	fanning friction factor for developing turbulence flow	α	phase saturation
F	pressure factor	γ	packing void fraction (porosity)
$\vec{F}_{D,i}$	mechanical dispersion force of phase *i*, $N \cdot m^{-3}$	β	dynamic contact angle
$\vec{F}_{disp,i}$	total dispersion force of phase *i*, $N \cdot m^{-3}$	β_1	characteristic dynamic contact angle (=75°), °

$\vec{F}_{drag,i}$	interaction force between the phase i and solids of the packing material, $\mathrm{N \cdot m^{-3}}$	ε	volume fraction
g_c	centrifugal acceleration, $\mathrm{m \cdot s^{-2}}$	$\nabla\varepsilon_i$	spatial gradient of the phase volume fraction
g_1	characteristic centrifugal acceleration (=205.6 $\mathrm{m \cdot s^{-2}}$), $\mathrm{m \cdot s^{-2}}$	σ	surface tension, $\mathrm{N \cdot m^{-1}}$
K_{iS}	porous resistance coefficient between the phase and solid	θ	angle of flow direction slop to the bed axis, °
K_{GL}	momentum exchange coefficient between the gas and liquid	ρ_i	density of phase i, $\mathrm{kg \cdot m^{-1}}$
L	length, m	μ	dynamic viscosity, $\mathrm{kg \cdot m^{-1} \cdot s^{-1}}$
L_e	effective flow length, m	τ	bed tortuosity factor
N	rotational speed, rpm	$\bar{\bar{\tau}}$	stress tensor
P	pressure, Pa	ν	kinematic viscosity, $\mathrm{m^2 \cdot s^{-1}}$
P_c	capillary pressure, Pa	ν_1	characteristic kinematic viscosity (=3.35 × 10^{-6} $\mathrm{m^2 \cdot s^{-1}}$), $\mathrm{m^2 \cdot s^{-1}}$
ΔP	pressure drop (flow resistance), Pa	ϕ	particle shape factor
Q	volume flow rate, $\mathrm{m^3 \cdot s^{-1}}$	*Subscripts*	
Re_K	Reynolds number	C	capillary pressure
S_f	spread factor, m	*disp*	dispersion force
$\vec{S}_{GL}$	interfacial force between the gas and liquid, $\mathrm{N \cdot m^{-3}}$	G	gas phase
t	time, s	i	=G, L
u_0	superficial velocity, $\mathrm{m \cdot s^{-1}}$	L	liquid phase

u_e	effective velocity, $\mathrm{m \cdot s^{-1}}$	S	solids phase for the packing materials
$\vec{u}_i$	velocity of phase i, $\mathrm{m \cdot s^{-1}}$	w	wire mesh
U	average superficial liquid velocity, $\mathrm{m \cdot s^{-1}}$		

1. Introduction

The rotating packed bed (RPB) is one of the many novel multi-phase contactors and reactors that can reduce the size of the packed bed because the mass transfer can be much improved due to the centrifugal force (100-1000 times that of gravity) that is exerted (Adamu et al., 2020; Cortes Garcia et al., 2017, 2021; Ghadyanlou et al., 2021). Due to the effect of the centrifugal force, the surface renewal of the phases (such as gas-liquid, liquid-liquid, gas-liquid-solid) in the packing is enhanced, which results in a significant increase in the overall mass transfer (Ouyang et al., 2018b; Wang et al., 2019; Wenzel and Górak, 2018b; Yang et al., 2019). There are many kinds of RPBs, and, at present, the single block counter-current flow RPB is the most popular, see Figure 1. The liquid (blue arrow) that enters from the liquid distributing nozzle, located at the center of the RPB impacts on the packing, then the liquid spreads out and splits into small droplets, or forms thin films on the packing surface on the way outwards through the RPB. The process is driven by the centrifugal force generated by the rotation of the RPB. Then, the liquid with large velocity resulting from the rotation of the bed flows into the outer cavity zone in the form of droplets and hits on the casing wall. Finally, the liquid flows out from the liquid outlet under the effect of gravity. Simultaneously the gas phase (yellow arrow) from the inlet, which is located at the outer radius of the RPB, flows inwards through the packing and it interacts with the liquid phase on its way to the gas outlet at the centre of the RPB. The liquid holdup (the volume of liquid held per volume of the packing) and its flow patterns passing the packing have a major impact on the gas-liquid mixing and the effective interfacial area it creates between the gas and liquid, which directly influences the mass transfer

performance of the RPB (Wenzel et al., 2018a). Thus, the study of the liquid flow dynamics is extremely important for the RPB analysis.

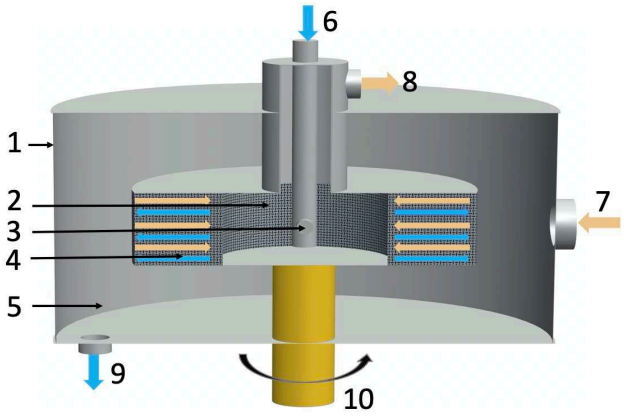

Figure 1. Schematic of a typical RPB with a single block counter-current flow arrangement (1. Casing; 2. Inner cavity zone; 3. Liquid nozzle; 4. Packing; 5. Outer cavity zone; 6. Liquid inlet; 7. Gas inlet; 8. Gas outlet; 9. Liquid outlet; 10. Motor).

Due to the strong centrifugal force and the narrow flow channel, the flow dynamics in the RPB is very complex. When the liquid enters the rotating packing, with a radial velocity only, it hits against with the rotating porous packing violently and the liquid is quickly dispersed, some of the liquid is attached to the packing surface and some eventually splits into numerous tiny droplets. This process forms a large interfacial surface area and renews them quickly (Wang et al., 2021). The mixing at the entrance is very strong, which is called the “end-effect” zone (Luo et al., 2012a; Ouyang et al., 2019; Yi et al., 2009). After that, the liquid achieves its tangential velocity, and its motion becomes largely synchronized with the rotating packing in the bulk of the packing region (Guo et al., 2017). As a result, the liquid dispersion is relatively weak compared with that in the end-effect zone. Throughout the RPB, liquid dispersion due to its interaction with the packing plays an important role in determining the liquid flow behaviour in the RPB and it is the predominant reason for the enhancement of the mass transfer in RPBs (Zhang et al., 2017).

Liquid dispersion in the RPBs has been explored previously both experimentally and computationally using the Volume of Fluid (VOF) method. For example, the dispersion

phenomenon of a liquid jet impacting on a rotating single-layer wire mesh has been visually examined under the effect of gravity and centrifugal force (Lu et al., 2019b; Wang et al., 2021; Xu et al., 2019; Zhang et al., 2020). In addition, the influence of the surface wettability and the liquid velocity, etc. on the liquid dispersion in the RPB have been analyzed in (Lu et al., 2019b; Ma et al., 2019; Su et al., 2020; Zhang et al., 2017). However, the above studies were only at the stage of observing the phenomenon and the process of the dispersion in RPBs, and no one has evaluated and quantified the dispersion in a RPB.

In addition, 2D and mesoscale 3D models with the VOF method have been employed to study the micromixing and liquid holdup in the packing region of a small RPB (Guo et al., 2016; Liu et al., 2020; Ouyang et al., 2018c; Shi et al., 2013; Xie et al., 2019; Yang et al., 2016). The VOF model could clearly capture the gas-liquid contact surface. However, it can only be used for analysing very small lab-scale RPB models and it will become computational prohibitively expensive to be used for the simulations of large RPBs because of the limitations in the computational resources and simulation times (Liu et al., 2017; Xie et al., 2019; Yang et al., 2010). For instance, about 1.4 million cells and a simulation time of about 60 h were required for each case in the 2D work of Guo et al. (2016), in which the inner and outer diameters of the packing simulated were only 80 and 140 mm, respectively. Therefore, for the purpose of future scaling up and optimization of the RPB, a different modelling approach must be developed. In our previous publications, Lu et al. (2018, 2019a) have proposed the use of the Eulerian method to study the flow dynamics where a new porous model for the RPB has been proposed and the effectiveness of the model has been demonstrated in a 2D RPB. The focus of this paper will be on the modeling of the effect of liquid dispersion and to extend the work into 3D.

The Eulerian method with the porous medium model is not able to resolve the matrix structure of the packing in detail (Pham et al., 2015b). Instead, the packing is considered as a porous medium and its effect on the flow is considered computationally using a

suite of mathematical formulations. This can substantially reduce the complexity and number of the cells in the computational mesh that is employed, thus leading to a significant reduction in the computational resources and simulation times required and make it possible to be used to simulate the full scale RPB using CFD for the scaling up and process optimization (Lu et al., 2019a).

The Eulerian porous medium model (Lu et al., 2018, 2019a) treats the gas and liquid as two continuous but penetrable phases. In order to employ the Eulerian porous medium model to investigate the liquid dispersion, a dispersion model needs to be devised to calculate the dispersion force term as a consequence of the volume averaging in the momentum equations (Boyer et al., 2005). Currently, there has been no dispersion model developed specifically for RPBs. However, various such models have been proposed for the modelling of the liquid dispersion in the conventional packed beds (CPBs). These models may be divided into the capillary pressure models and mechanical dispersion models according to the dispersion mechanism that they model in the CPBs (Wang et al., 2013). The capillary pressure force is produced by the difference in the pressures across the fluid interface. In addition, the mechanical force is caused by the complex advection of the momentum by the fluid at the pore scale (Fourati et al., 2013) or, in other word, the variation in the velocity with respect to the main flow at the macroscopic scale (Carney and Finn, 2016). It should be noted that the nature and structure of the porous media packing employed in the CPBs and RPBs are very different. Usually, a wire mesh packing or a nickel foam packing is employed in the RPBs, while a more structured packing or random packing elements are employed in the CPBs. In addition to the nature of the packing types, the packing in an RPB is much more densely packed than that in CPBs. The driving force and the flow patterns are also very different. Nevertheless, we take the view that both CPB and RPB are similar in that they both can be regarded as being a porous media and the liquid disperses from a higher volume fraction to a lower volume fraction under the framework of the porous medium approach. The macro dispersion mechanisms are

similar in RPBs and CPBs. Hence, it is expected that these dispersion models for CPBs could be employed in RPBs with careful evaluations. One of the main objectives of this paper is to assess the suitability and limitations of the existing dispersion models when they are applied to model the RPBs. More information about these models is given in Section 2.5.

In this paper, a 3D RPB model was developed based on a practical RPB from the published literature. The packing zone was regarded as a porous media and the Eulerian porous medium method coupled with the interfacial, drag and dispersion forces models were employed to study the liquid dispersion in the packing region of the RPB. The results have been compared with the available experimental data. The sensitivity of the sub-models and the effect of some important parameters, including the rotational speed, bed porosity, liquid flow rate, liquid nozzle size and number of nozzles have been thoroughly analyzed and discussed. The results show that using the model developed can accurately reflect the distribution of the liquid holdup in the packing region and the effect of the dispersion force on the liquid holdup under different simulation conditions. Thus, the proposed method has paved the way for the model to be used, with confidence, in the future for simulating the gas-liquid flow in a 3D full-scale RPB cost effectively and accurately.

2. CFD simulations

2.1 Geometry of the RPB

In order to develop and validate the CFD model, a good set of quality experiment data should be obtained. Among all the available experimental studies in the literature on RPBs (Burns et al., 2000; Liu et al., 2020; Wenzel et al., 2018a; Yang et al., 2015a), Yang's experimental data (Yang et al., 2015a) has been selected. This is because of the following reasons: (i) the relative detailed dimensions of the RPB have been provided, especially the size of the liquid distribution nozzle; (ii) the packing material used in Yang's experiment matches those employed in the development of the drag force model used in this paper so that the accuracy of the model can be established; (iii) the liquid

holdup with different operational conditions and the distribution of liquid holdup along the radial position are presented in Yang's paper, which could be used to verify the simulation results; and (iv) the experimental data has been previously used by Ouyang et al. (2018c), Lu et al. (2018), Xie et al.(2019) and Liu et al. (2020) in order to validate their models, thus indicating that the data is reliable.

The 3D geometry of the experimental rig has been reproduced in Figure 2. Because the outer cavity zone between the case and the rotating bed has almost no influence on the liquid holdup within the packing region (Xie et al., 2017; Yang et al., 2016), and the objective of this paper is to study the hydrodynamics in the packing region, then only the rotating bed itself and the location of the liquid nozzle are shown in the figure. The inner diameter, outer diameter and axial length (thickness) of the packing are 42, 82 and 20 mm, respectively. The packing is a wire mesh with a void fraction and a specific area of 0.95 and 497 m^2/m^3, respectively. The rotational speed of the bed employed in the experiments varied between 500-2500 rpm, and the liquid flow rate ranged from 22.9 - 43 cm^3/s. The liquid distributing nozzle is rectangular in shape, and its size is 1×15 mm.

In the CFD model, due the symmetry of the packing bed, only half of the bed has been investigated, and the thickness of the packing is 10 mm, as shown in Figure 2. In addition, for the purpose of numerical stability, an 8mm extension to the exit of the rotational bed was used. Therefore, the diameter of the model is 90 mm in total.

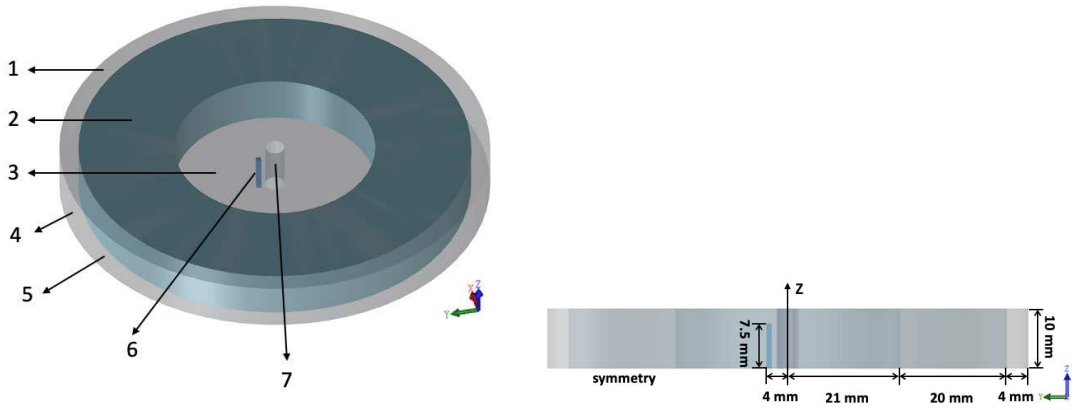

Figure 2. Schematic diagram of the 3D RPB and corresponding size (1, outer cavity zone; 2, packing zone; 3, inner cavity zone; 4, pressure outlet; 5, symmetry; 6, liquid inlet; 7, pressure outlet, Z - axis is the axis of rotation).

2.2 Governing fluid flow equations

The main assumptions made for the RPB model are as follows:

(i) The packing is a homogenous porous medium.

(ii) The flow is incompressible.

(iii) The pressure field is shared by the gas and liquid phases.

(iv) The liquid flow in the packed bed is dominated by the form of the film, and the dispersed droplets.

The continuity equation describing the overall mass conservation is expressed as follows:

$$\frac{\partial}{\partial t}(\varepsilon_i \rho_i) - \nabla \cdot (\varepsilon_i \rho_i \vec{u}_i) = 0 \quad (1)$$

where ρ_i is the density (i = G for gas or L for liquid), t is the time, $\vec{u}_i$ is the fluid velocity, ε_i is the phase fraction, which is defined as follows:

$$\varepsilon_i = \alpha_i \gamma = \frac{V_i}{V_G + V_L}\gamma = \frac{V_i}{V_G + V_L + V_S} \quad (2)$$

where α_i is the phase saturation ($\alpha_i = \frac{V_i}{V_G + V_L}$), γ is the porosity of the packing, V_i is the volume of the ith phase, V_S is the solid volume of the wire mesh, and the subscripts G, L, S indicate the gas, liquid, and solid phase, respectively.

The momentum conservation equation includes the convection force, the pressure force, the viscous force, the drag force, the interfacial force, and the dispersion force. The body force is neglected in the absolute frame of reference that is employed in the paper. Therefore, the governing momentum equations of the fluid flow are as follows:

$$\frac{\partial}{\partial t}(\varepsilon_L \rho_G \vec{u}_L) + \nabla \cdot (\varepsilon_L \rho_L \vec{u}_L \vec{u}_L) = -\varepsilon_L \nabla P + \varepsilon_L \nabla P_c + \nabla \cdot (\varepsilon \bar{\bar{\tau}}_L) - \vec{F}_{drag,L} + \vec{S}_{GL} + \vec{F}_{disp,L} \quad (3)$$

$$\frac{\partial}{\partial t}(\varepsilon_G \rho_G \vec{u}_G) + \nabla \cdot (\varepsilon_G \rho_G \vec{u}_G \vec{u}_G) = -\varepsilon_G \nabla P + \nabla \cdot (\varepsilon \bar{\bar{\tau}}_G) - \vec{F}_{drag,G} - \vec{S}_{GL} + \vec{F}_{disp,G} \quad (4)$$

where P is the pressure, P_c is the capillary pressure, which is only included in the liquid phase momentum equation, $\bar{\bar{\tau}}_i$ is the stress tensor, $\vec{F}_{drag,i}$ is the drag force between the fluid and packing, $\vec{S}_{GL}$ is the interfacial force between the gas and liquid, and $\vec{F}_{disp,i}$ is the mechanical dispersion force.

2.3 Drag force and interfacial force models

Resolving the complex geometry of the packing structure at the pore scale is computationally not feasible. Instead, the packing structure is replaced with an effective porous medium. It is very important to determine a correct resistance force model for the porous medium in order to describe the gas-liquid interfacial force and phase-solid drag force accurately, since it substantially influences the liquid holdup and the pressure drop (Kołodziej and Łojewska, 2009). Although various porous medium resistance force models, such as those for spherical packing (Attou et al., 1999; Ergun, 1952; Lappalainen et al., 2008), structured slit packing (Iliuta et al., 2014), and tube bundle packing (Zhang and Bokil, 1997), have been proposed, Lu et al. (2018) illustrated that these models failed to predict the practical liquid holdup in the wire mesh packing, thus indicating that these models were not suitable for the RPBs (Bussière et al., 2017). In 2009, Kołodziej and Łojewska (2009) put forward a one-phase model that takes into account both the viscous and inertia contributions to the overall resistance of the wire meshed porous media, based on single flow experiments through wire gauzes, which is similar to that of the flow through a wire mesh packing in RPBs. Subsequently,

Kołodziej et al. (2012) introduced another form of the porous resistance model by redefining the effective length and effective velocity of the liquid flow in the packing region, and suggested the following pressure drop equations:

$$\frac{\Delta P}{L} = 4(f_l + f_t)\frac{\rho u_0^2}{2d_w}\frac{1-\gamma}{\gamma^3}\frac{\tau^2}{cos\theta} \tag{5}$$

$$L_e = \frac{L}{cos\theta}, u_e = \frac{u_0\tau}{\gamma} \tag{6}$$

where ΔP is the pressure drop, L and L_e are the length/depth of the packing and the effective flow length, respectively, u_0 and u_e are the superficial velocity and effective velocity, respectively, f_l and f_t are the Fanning factors for the laminar and turbulent flows, respectively, d_w is the diameters of the dry wires, τ is the tortuosity factor resulted from the tortuous path that the fluid passes through, θ is the angle between the axis of the packing and the direction of the fluid flow which is influenced by the orientation of the packing. This resistance model is a good improvement over the previous model (Kołodziej and Łojewska, 2009) proposed by Kołodziej and Łojewska because the liquid residence time ($t = \frac{L_e}{u_e} = \frac{L\gamma}{u_0 cos\theta\tau}$) usually increases after considering the influence of the tortuous path and the orientation of the packing. It is also proved that using this model produces results, which are in much better agreement with the experimental data (Bussière et al., 2017).

When the liquid passes through the wire mesh in the RPB, some of the packing surface is covered by the liquid film, this is noted as the wet area $(a_s \times f_e)$, and the remaining area of the packing is covered by the gas, noted by the dry area, $a_s \times (1 - f_e)$. f_e is the fraction of the wetted area of the packing, and it is defined as the ratio of the wetted interfacial area A_{GL} to the total packing surface area:

$$f_e = \frac{A_{GL}}{a_S} \tag{7}$$

The wetted interfacial area A_{GL} needs to be modelled and this will be discussed later

in Section 2.5.

The drag force between the gas and the solids, the liquid and the solids, as well as the interfacial force between the gas and the liquid can be expressed as follows (Kołodziej and Łojewska, 2009; Lu et al., 2018, 2019a):

$$\vec{F}_{drag,L} = K_{LS}\vec{v}_L = f_e\varepsilon_L\vec{v}_L\left[4(f_l + f_t)\frac{\rho_L|\vec{v}_L|}{2d_w}\frac{\varepsilon_S}{\varepsilon_L}\frac{\tau^2}{cos\theta}\right] \tag{8}$$

$$\vec{F}_{drag,G} = K_{GS}\vec{v}_G = (1 - f_e)\varepsilon_G\vec{v}_G\left[4(f_l + f_t)\frac{\rho_G|\vec{v}_G|}{2d_w}\frac{(1-\varepsilon_G)}{\varepsilon_G}\frac{\tau^2}{cos\theta}\right] \tag{9}$$

$$\vec{S}_{GL} = K_{GL}(\vec{v}_G - \vec{v}_L) = f_e\varepsilon_G(\vec{v}_G - \vec{v}_L)\left[4(f_l + f_t)\frac{\rho_G|\vec{v}_G - \vec{v}_L|}{2d'_w}\frac{(1-\varepsilon_G)}{\varepsilon_G}\tau^2\right] \tag{10}$$

$$f_l = \frac{1}{Re_K}\left(\frac{3.44}{\sqrt{\mathcal{X}^+}} + \frac{\frac{1.25}{4\mathcal{X}^+} + 16 - \frac{3.44}{\sqrt{\mathcal{X}^+}}}{1 + \frac{0.00021}{\mathcal{X}^{+2}}}\right) \tag{11}$$

$$f_t = \frac{0.079}{Re_K^{0.25}} \tag{12}$$

$$\mathcal{X}^+ = \frac{d_w}{D_h Re_K} \tag{13}$$

$$Re_K = \frac{\rho v_e D_h}{\mu} \tag{14}$$

For the fluid-solids interaction:

$$\tau = 1 + \frac{\varepsilon_S}{2}\ , d_w = \frac{4\varepsilon_S}{a_S}, v_e = \frac{|\vec{v}'_i|\tau}{\varepsilon_i}, D_h = \frac{4\varepsilon_i}{a_S}, \vec{v}_L = \frac{\vec{v}'_i}{\varepsilon_i} \tag{15}$$

For the gas-liquid interaction:

$$\tau = 1 + \frac{\varepsilon_S + \varepsilon_L}{2}, d'_w = \frac{4\varepsilon_S}{a'_S}, v_e = \frac{|\vec{v}'_G - \vec{v}'_L|\tau}{\varepsilon_G}, D_h = \frac{4\varepsilon_G}{a'_S}, a'_S = \left(\frac{\varepsilon_S}{\varepsilon_S + \varepsilon_L}\right)^{0.5} a_S \tag{16}$$

where $\vec{F}_{drag,G}$, $\vec{F}_{drag,L}$ and $\vec{S}_{GL}$ are the drag forces between the gas and the solids, the liquid and the solids and the interfacial force between the gas and the liquid, respectively; K_{GS}, K_{LS} and K_{GL} are the porous resistance coefficients between the gas and the solids, the liquid and the solids and the momentum exchange coefficient between the gas and the liquid, respectively; d'_w is the diameter of the wet wires, D_h

is the hydraulic diameter, Re_K is the Reynold number, $\vec{v}_i$, $\vec{v}_i$ and $\vec{v}_e$ are the local superficial velocity, local velocity and effective velocity relative to the rotating packing, respectively; μ is the viscosity, a_S and a_S' are the specific area of the dry packing and the wet wires, respectively. It is difficult to directly obtain the value of θ in this work because of the complexity in the stack screen packing. However, this angle may be obtained by an indirect approach, which is through the validation of the simulation results with the experimental data. For example, Lu et al. (2018) and Bussière et al. (2017) obtained the angle through the validation of the simulation results with the experimental data on the liquid holdup distributions and pressure drop, respectively. Similarly, different values of θ have been tested in this paper and the obtained liquid holdup has been compared with the experimental data. The larger the value of θ, the higher is the liquid holdup, which means more liquid holdup has been captured within the RPB (Lu et al., 2019a). When the angle is set as 83.95°, the simulation results have the best agreement with the experimental data.

2.4 Dispersion force

As mentioned previous, in two-phase flows through porous media, the dispersion terms appear in the governing fluid flow equations due to the volume averaging of the momentum equations. The dispersion terms mainly result from two distinct mechanisms: capillary pressure and mechanical dispersion. Popular models for these two mechanisms for CPBs, and also assessed in this paper for the RPB, are as follows:

2.4.1 Capillary pressure

For the capillary pressure, in general, two models have been used, i.e. the Grosser model and the Attou and Ferschneider model. The model of Grosser et al. (1988) was introduced through a permeability concept based on the Leverett's function. The Attou and Ferschneider model (Attou and Ferschneider, 1999) considers the loss of stability of the liquid film on the particle surface at the pore scale. The Grosser and Attou capillary pressure models are presented in Equations 17 and 18, respectively, as follows:

$$P_c = \frac{1-\gamma}{\gamma d_w}\sqrt{180}\sigma\left[0.48 + 0.036ln\left(\frac{1-\varepsilon_S-\varepsilon_L}{\varepsilon_L}\right)\right] \quad (17)$$

$$P_c = 2\sigma\left(\frac{1-\gamma}{1-\varepsilon_G}\right)^{\frac{1}{3}}\left(\frac{1}{d_w}+\frac{1}{d_{min}}\right)F\left(\frac{\rho_G}{\rho_L}\right) \quad (18-\text{a})$$

$$d_{min} = \left(\frac{\sqrt{3}}{\pi}-\frac{1}{2}\right)^{\frac{1}{2}} d_w \quad (18-\text{b})$$

$$F\left(\frac{\rho_G}{\rho_L}\right) = 1 + 88.1\left(\frac{\rho_G}{\rho_L}\right) \ \left(\text{for } \frac{\rho_G}{\rho_L} < 0.025\right) \quad (18-\text{c})$$

where σ is the surface tension. Further, these models can be modified by considering the fraction of the wetting area of the packing, f_e (Jiang et al., 2002) as follows:

$$P_G - P_L = (1-f_e)P_c \quad (19)$$

where $P_G - P_L$ is the modified capillary pressure between the gas and liquid phase. These models have been used to analyze the effect of the capillary pressure on the radial liquid distribution in CPBs (Boyer et al., 2005; Gunjal et al., 2005; Solomenko et al., 2015; Wang et al., 2013). However, most investigators tend to ignore the capillary pressure due to the large particle size and high packing porosity (Fourati et al., 2013) in the CPB, and the mechanical dispersion was the only dispersion force that has been considered in their investigations (Kim et al., 2016, 2017; Pham et al., 2015b).

2.4.2 Mechanical dispersion

Liu and Long (2000), Mewes et al. (1999) and Lappalainen et al. (2009) have proposed many mechanical dispersion models for the CPBs. Among these models, the model proposed by Lappalainen et al. (2009) is the most popular, and it has been employed in many works for the CPB simulations (Kim et al., 2016, 2017; Pham et al., 2015a, 2015b). This model was initially derived based on spherical particle packings, and then it was proven to be suitable for structured packings (Fourati et al., 2013; Iliuta et al., 2014), thus indicating that this model has a wide range of adaptability to model the flow in different types of packings. Hence, the original model of Lappalainen et al. (2009) is considered in this paper to take into account the liquid dispersion in the RPB, which can be expressed as follows:

$$\vec{F}_{D,G} = K_{GS}\vec{v}_{D,G} + K_{GL}\left(\vec{v}_{D,G} - \vec{v}_{D,L}\right) \quad (20)$$

$$\vec{F}_{D,L} = K_{LS}\vec{v}_{D,L} - K_{GL}\left(\vec{v}_{D,G} - \vec{v}_{D,L}\right) \quad (21)$$

where $\vec{F}_{D,i}$ is the mechanical dispersion force for the *i*th phase, and $\vec{v}_{D,i}$ is the drift velocity for the *i*th phase.

Based on the Fickian assumption, the drift velocity is a function of the gradient of the phase volume fraction and a spread factor, S_f. It can be written as follows:

$$\vec{v}_{D,L} = -\frac{S_f}{\varepsilon_L}\left(|\vec{v}_L|\nabla\varepsilon_L - (\vec{v}_L \cdot \nabla\varepsilon_L)\frac{\vec{v}_L}{|\vec{v}_L|}\right) \tag{22}$$

$$\vec{v}_{D,G} = -\frac{S_f}{\varepsilon_G\alpha_G}\left(|\vec{v}_G|\nabla\varepsilon_G - (\vec{v}_G \cdot \nabla\varepsilon_G)\frac{\vec{v}_G}{|\vec{v}_G|}\right) \tag{23}$$

$$S_f = 0.231{d_w}^{0.5}\sigma \tag{24}$$

where $\nabla\varepsilon_i$ is the spatial gradient of the phase volume fraction, and σ is the surface tension.

Compared with the liquid dispersion force, the gas dispersion force is very small and has little effect on the liquid flow dynamics. More importantly, there is no forced gas flow in the RPB model used in this paper; therefore, the gas dispersion force (equation (21)) may be neglected. Furthermore, since the gas-liquid momentum exchange coefficient K_{GL} in Equations (20-21) is extremely small compared with the liquid-solid porous resistance coefficient K_{LS}, equation (22) can be reduced to

$$\vec{F}_{D,L} = K_{LS}\vec{v}_{D,L} \tag{25}$$

This is the most important force term in the liquid mechanical dispersion force, which has been verified in previous numerical studies (Fourati et al., 2013).

2.5 Gas-liquid effective interfacial area

The gas-liquid effective interfacial area (wetted interfacial area) is a critical parameter that has to be modelled when using porous medium models. Various empirical equations for the effective interfacial area have been derived for CPBs and they have been utilized for RPBs simulation by replacing the acceleration force term is the equation with the centrifugal force in the RPBs (Kang et al., 2014, 2016; Lu et al., 2018). This often results in an underestimation of the value of the effective interfacial area. The fraction of the interfacial area has been estimated in the RPB for CO_2 capture experiments (Guo et al., 2014; Luo et al., 2012b, 2017; Zheng et al., 2016). However,

the accuracy of the model is affected by the absorption rate of CO_2, partial pressure of CO_2 in the gas phase, and diffusivity of CO_2 in solution, etc. Therefore, it is not completely reliable.

In our recent publication, Xie et al. (2019) have estimated the effective interfacial area when the liquid flows over a RPB packing material using the VOF modelling method by considering a range of different gravitational acceleration forces. The model has been validated against experimental observations and a correlation for the interfacial area was proposed as follows:

$$A_{GL} = 202.3485\left(\frac{g_c}{g_1}\right)^{0.0435}\left(\frac{U}{U_1}\right)^{0.4275}\left(\frac{\nu}{\nu_1}\right)^{0.1200}\left(\frac{\beta}{\beta_1}\right)^{-0.5856} \quad (26)$$

where the experimental constants g_1 = 205.6 m/s^2, U_1 = 0.0106 m/s, ν_1 = 3.35×10^{-6} m^2/s and β_1 = 75°; g_c is the central pedal acceleration, U is the average superficial liquid velocity, ν is the kinematic viscosity of the liquid, and γ is the dynamic contact angle, which is set as 26° in this work. In addition, the modelled fractional effective interfacial area by using equation (26) for the cases investigated in Section 3 is in the range of 0.38-0.68, which is reasonable based on the previous RPB experimental work (Luo et al., 2017; Yang et al., 2011). Therefore, this correlation will be employed in this paper and the average superficial velocity should be replaced by the local superficial velocity as follows:

$$U = \varepsilon_L|\vec{v}_L| \quad (27)$$

2.7 CFD model setup

The 3D RPB simulations have been performed using the ANSYS Fluent (version 2019R3). The ANSYS Mesh was employed to generate the grid of the 3D RPB model, see Figure 3 for a typical mesh layout. The hexahedral mesh elements formed the 3D computational grid. The average skewness and element quality are 0.09 and 0.91, respectively. The liquid holdup in the packing was tested with many different numbers of cells and meshes in order to obtain a mesh independent solution. As a result, 51,000 cells were employed in order to accurately calculate the flow field.

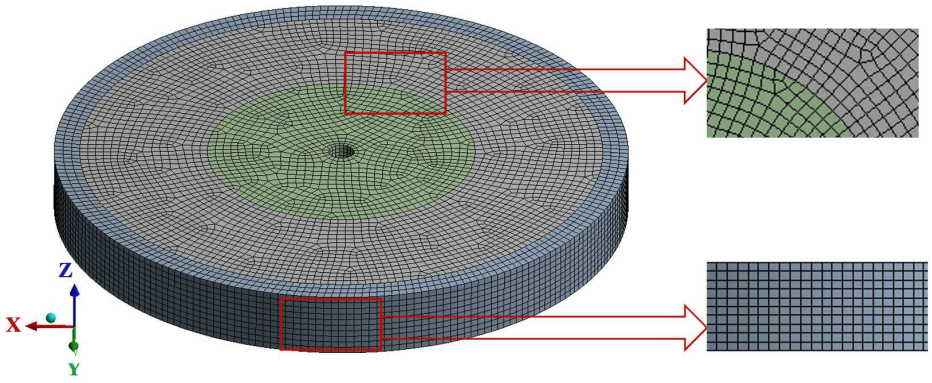

Figure 3. Schematic of the mesh in the 3D model.

The transient based solver is employed in order to solve the governing fluid flow equations discussed in the previous sections and various user-defined-functions (UDFs) have been developed for implementing the extra forces in the momentum equations. The air and water have been selected as the gas and liquid materials, respectively.

It is generally believed that the realizable k-ε model is more suitable for RPB than the standard k−ε model due to two reasons. Firstly, the realizable k-ε model contains a new formulation for the turbulence viscosity: C_μ is not a constant as in the standard model but a variable, and it is a function of the mean strain and rotation rates (Shih et al., 1995). The second reason is a new transport equation for the dissipation rate in the realizable k-ε model, ε, is employed and this is derived from an exact equation for the transport of the mean-square vorticity fluctuation (Lateb et al., 2013). As a result, the realizable k-ε model gives improved predictions for the spreading rate of the jets, a superior ability to capture the mean flow of complex structures and for flows involving rotation, boundary layers under strong adverse pressure gradients, separation and recirculation (Yang et al., 2010). In addition, it has been frequently used for the fluid flow simulations in RPBs (Liu et al., 2017; Ouyang et al., 2018c; Wang et al., 2020; Wu et al., 2018; Yang et al., 2015b). Therefore, the realizable k-ε turbulence model has been chosen in this study.

The pressure-based method and the absolute velocity formulation have been utilized. The time step was set as 3×10^{-4} s, and the maximum iteration number was less than 20

at each time step and the convergence tolerance was 1×10^{-4}. When the simulation achieved the pseudo steady state, the difference of the mass flow rate between the liquid inlet and outlet was less than 0.1%, and the residuals of the mass balance equations and the other equations were less than 5×10^{-4} and 1×10^{-4}, respectively.

It can be seen from Figure 2 that the liquid inlet (boundary 6) has been set as a velocity inlet boundary and it ranges from 1.53 to 2.87 m/s according to the experimental settings (Yang et al., 2015a). In addition, there is no forced gas flows through the packed bed in the experiment (Yang et al., 2015a). Accordingly, the inner and outer surfaces of the RPB (boundary 7 and 4) are set as pressure outlets with a zero gauge pressure. Since the gravity is relatively small when compared with the high centrifugal force (5.8-286 times that of gravity), the gravity can be neglected in the RPB (Ouyang et al., 2018a) and the flow is almost symmetric across the bed from the top to the bottom. Therefore, only half of the bed has been modelled with a symmetric boundary being applied on the central plane perpendicular to the rotating axis in order to minimize the computational time. The sliding model has been employed to realize the motion of the packing. The wall boundaries have been set as no slip walls.

3. Results and discussion

In this section, the model validations have been presented with one of the experimental cases and a total of 96 cases have simulated where the sensitivity of the formula employed for the modelling of the dispersion force and the effect of various design and operational parameters of the RPB on the fluid flows and liquid holdups have been investigated.

Table 1. The operational conditions for the baseline case for the model validation (Yang et al., 2015a).

Liquid flow rate (cm^3/s)	Liquid viscosity (kg/(m· s))	Rotational speed (rpm)	Packing porosity	Nozzle size (mm×mm)	Number of nozzles
43	0.001	1500	0.95	15×1	1

3.1 Validation and the liquid holdup along the radial direction

In order to validate the CFD model developed, the liquid holdup has been chosen as the validation parameter because of the following reasons: (i) the liquid holdup is one of the most important parameters in packed bed design, as it is relevant to the hydraulic and mass transfer property of the bed. It is a result of the balance of various forces including the dispersion force acting on the liquid; (ii) the liquid holdup could indirectly reflect other factors, such as the liquid velocity. For the RPBs, the higher the radial velocity, the lower is the liquid holdup. If the liquid holdup obtained by the simulation matches well with the experimental data, then this indicates that the liquid velocity has a good agreement with the experimental data; (iii) although many parameters, including the liquid holdup, liquid velocity, etc., could be obtained by the simulation, the liquid holdup is much easier to be obtained for most experimental investigations. Therefore, many studies on the flow dynamics in the RPBs have selected the liquid holdup as the validation parameter (Liu et al., 2020; Lu et al., 2018; Ouyang et al., 2018c, 2019; Xie et al., 2017; Zhang et al., 2020). The distributions of the liquid holdup, and the fractional effective interfacial area in the RPB have been obtained under the conditions of 1500 rpm rotational speed and 43 cm^3/s liquid flow rate, as listed in Table 1. The results obtained are compared with the experimental data obtained from (Yang et al., 2015a).

Figure 4(a) shows the experiment observations obtained using X-ray technology, which shows the image of the liquid across the thickness of the bed. Figure 4(b) shows the predicted distribution of the liquid holdup on the central plane (plane of symmetry) obtained from the CFD simulation. A liquid stream with a high liquid fraction is presented in Figure 4(a) and 4(b) at the entrance to the bed due to the significant resistance of the packing. In addition, the liquid begins to flow in the tangential direction followed by the rotational bed and its radial velocity becomes larger under the effect of the centrifugal force. In the meantime, the liquid spreads and disperses along its flow path, resulting in a decreasing local liquid fraction and a more uniform liquid distribution as shown in both figures. The liquid volume fraction continues to decrease

until the liquid flows out the outer packing region. From the above analysis, it is known that the liquid flow process and the liquid holdup distribution within the RPBs are similar in the simulation results and experimental data. The quantitative comparisons will be given in Figure 5(b).

Figure 4(c) shows the predicted fractional effective interfacial area on the symmetric plane. Because the effective interfacial area is the interfacial area in contact with the gas and liquid, it can be found that the fractional effective interfacial area is larger where the liquid holdup is higher by comparing with Figures 4(b) and 4(c).

Figure 5 show the comparison of the liquid holdup between the simulation and the experimental data (Yang et al., 2015a) in terms of (a) the liquid holdup along the radial position and (b) the liquid total liquid holdup as a function of the rotating speed of the bed, together with the velocity distribution along the radial direction. From Figure 5(a), it can be seen that the liquid holdup increases in the inner packing region (end-effect zone) since more and more liquid is dispersed and captured and the liquid radial velocity decreases quickly as is shown on the left of Figure 5(c) and this results from the large resistance from the packing. After that, the liquid radial velocity increases gradually under the effect of the centrifugal force, and the liquid tangential velocity is close to and almost overlaps with the tangential velocity of the packing because the liquid quickly and largely follows the rotating packing after the liquid enters the packing. In the meantime, the fraction of the liquid volume (liquid holdup) should become smaller with the increase in the radial velocity and the flow space in the bulk and outer packing region, thus resulting in a gradually decreasing liquid holdup along the radial direction. This phenomenon has been accurately predicted by the simulation results and also in the experimental data except in the outer packing region where an increase in the holdups is observed in the experiments. As explained by the authors of the experiments (Yang et al., 2015a), the possible reasons of this observed increase are that the outer packing region has a slightly lower porosity relative to the bulk packing and the liquid droplets bounce back to the outer packing region after hitting the casing

wall. These two reasons lead to the observed increase in the liquid holdup in the outer packing region. In addition, these reasons could also explain the high liquid holdup in a thin ring observed experimentally at the outer packing in Figure 4(a).

Figure 5(b) shows the comparison of the liquid holdup in the packing region under different rotational speeds between the simulation results and experimental data. It can be seen that the two curves decrease with the increasing rotational speed due to the gradually stronger centrifugal force and the two curves are very close to each other. From Figure 5(b), the maximum deviation is observed at the lowest tested rotational speed (500 rpm) and the largest liquid flow rate (43 cm^3/s). However, for the rest of the test conditions, the deviation is much lower, which could even be as low as 2%. It can be seen from Figure 5(a) that the liquid holdup increases in the outer packing region in the experiment, which may be the main reason for the deviation. As explained in the last paragraph, the slightly lower porosity and the liquid droplets that bounce back into the outer packing region lead to the observed increase in the liquid holdup in the experiment (Yang et al., 2015a) and the deviation increases when the rotational speed decreases or the liquid flow rate increases. This could explain why the maximum deviation is observed at the lowest tested rotational speed (500 rpm) and the largest liquid flow rate (43 cm^3/s). In addition to the outer spacing region, the difference in the liquid holdup in the inner and bulk packing regions is relatively small. Although only one experimental work has been used to validate the work presented in this paper, the simulation results were very thoroughly and carefully compared with this set of experimental data. From Figures 4(a) and 4(b) as well as Figures 5(a) and 5(b), not only the distribution of the liquid holdup has been visually compared, but also the liquid holdup has been compared along the radial positions and under several different rotational speeds. Therefore, the model developed in this paper could be used with much confidence to investigate the flow dynamics in the RPBs.

Figure 6 shows the liquid distribution across the thickness of the bed on two different vertical planes (a, x=0 and b, y=0, see Figure 4(b)). It clearly can be seen from Figure

6(a) that after the jet flows from the liquid nozzle, the local liquid holdup becomes smaller in the inner cavity zone. When the liquid enters the inner packing, the local liquid holdup increases in the vicinity of the boundary of the inner cavity zone and the packing, and this increase has been shown and explained in Figures 4(a) and 4(b). After the liquid enters the packing, the liquid achieves its tangential velocity, thus, the liquid "appears and disappears" on these vertical planes as shown in Figures 6(a) and 6(b). Meantime, the liquid starts to disperse and spread, and as a result, the liquid distribution is relatively uniform in the axial direction in the outer packing region.

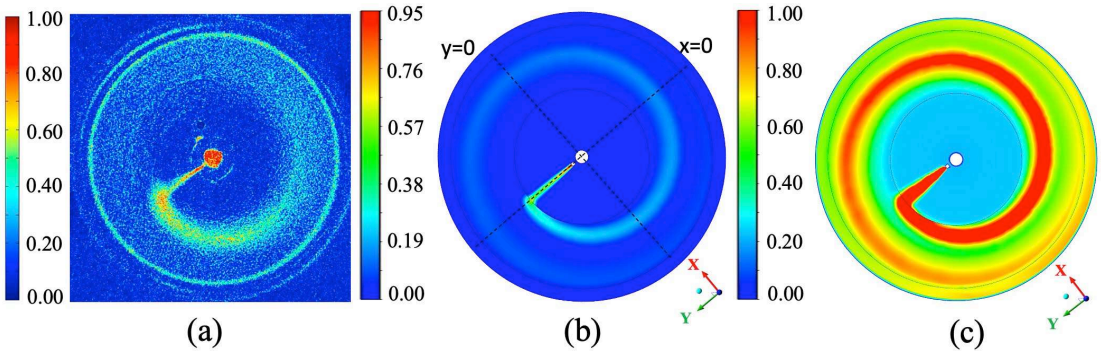

Figure 4. (a) Map of liquid holdup from the experiment (Yang et al., 2015a); contours of (b) liquid holdup from the simulation; and (c) fractional effective interfacial area from the simulation.

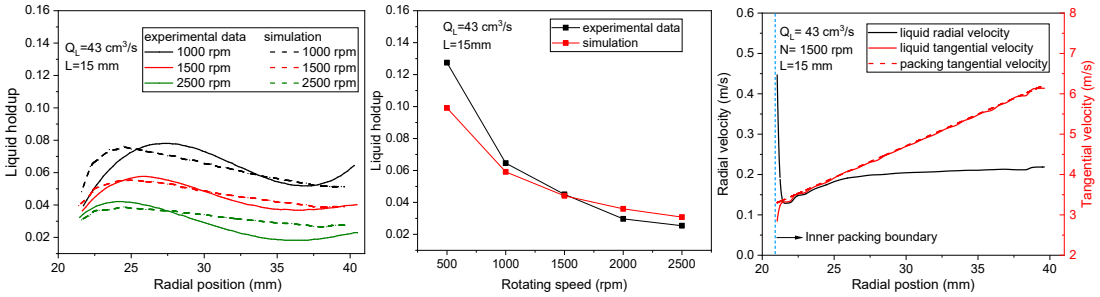

(a) (b) (c)

Figure 5. Comparison of the experimental data (Yang et al., 2015a) and the simulation results for the liquid holdup (a) along the radial direction; (b) under different rotational speeds; and (c) velocity components along the radial direction.

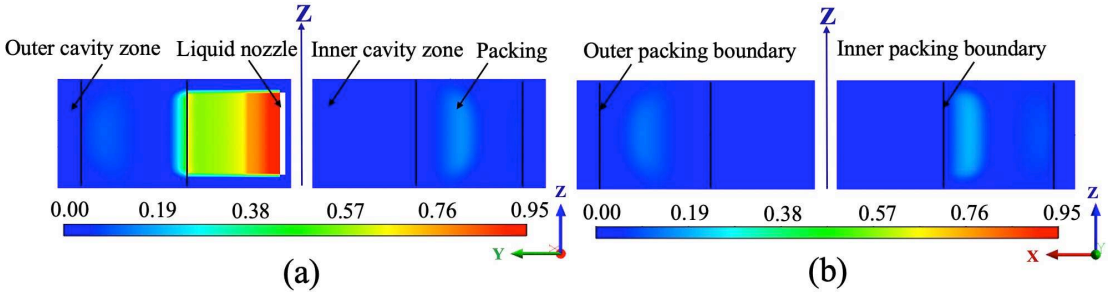

Figure 6. Contours of the liquid distribution on the planes (a) x = 0 and (b) y = 0.

3.2 Sensitivity of the simulation results to the dispersion force model

As mentioned in Section 2.4, the dispersion forces consist of the capillary pressure force and the mechanical dispersion force. Therefore, different capillary pressure models and the spread factor, S_f in the mechanical dispersion model can influence the magnitude of the modelled dispersion force and subsequently the distribution of the liquid holdup.

In order to demonstrate the degree of the liquid dispersion in all three flow directions, in particular the effect of the nozzle length. Two nozzle lengths, i.e. 15 and 7.5 mm (in the z-direction) have been employed.

(i) Capillary pressure model

The Grosser and the Attou and Ferschneider models, which have been introduced in Section 2.4 were, respectively, employed as a source term ($\vec{F}_{C,L} = \varepsilon_L(1 - f_e)\nabla P_C$) in the momentum equation and their effect on the predicted liquid holdup were compared

546 with those obtained without including the dispersion force term. In general, the liquid
547 will disperse from the region of a higher liquid volume fraction to the region of a lower
548 liquid volume fraction. During this process, the liquid spreads and disperses into
549 smaller droplets or forms thinner films under the effect of the dispersion force. This
550 subsequently leads to more contact between the liquid and the packing and this
551 increases the drag force from the packing (see Eq. 8). Therefore, more liquid is stacked
552 in the packing region and the liquid holdup increases.

553 Figure 7 shows the effect of two different capillary pressure models on the liquid holdup
554 distribution in the packing region for the two nozzle lengths investigated. It can be
555 observed in Figure 7 that the Grosser capillary pressure model (Eq. 17) has little effect
556 on the liquid holdup for both nozzle lengths. The possible reason is that in this model
557 the capillary pressure force is inversely proportional to the packing porosity and the
558 particle diameter only. Although the diameter of the wire mesh is small, the packing
559 porosity is large, and it is close to 1. In addition, it has been reported that this model
560 has the drawback that may fail to reproduce the steep rise in the capillary pressure as
561 the liquid saturation approaches zero (Lappalainen et al., 2009). The above reasons may
562 cause the Grosser capillary model to fail to catch the effect of the capillary pressure
563 force in this RPB model. However, an increase in the liquid holdup is shown in Figure
564 7 after employing the Attou model. This is because that the Attou model is not only
565 related to the packing porosity and diameter of the wire mesh, but also it is a function
566 of the minimum equivalent diameter (d_{min}) and the fluid density ratio. In addition, it
567 can be seen from Figure 7 that when the nozzle length is 15 mm, the liquid holdup starts
568 to increase in the inner packing region and this is because the liquid has enough contact
569 area with the packing to disperse due to the relatively uniform liquid distribution at the
570 axial direction (z - direction). However, when the nozzle length is 7.5 mm, which means
571 the liquid concentrates in the central part of the inner packing, the liquid dispersion
572 cannot increase quickly until it flows into the bulk of the packing where the liquid has
573 occupied enough space to disperse.

From the above analysis, it can be assumed that the Attou model can be used to accurately describe the capillary pressure force on the liquid holdup. In addition, this model can overcome the shortage of the Grosser model and it has been widely validated, and used in many works for CPBs (Lappalainen et al., 2009, 2011; Solomenko et al., 2015). Therefore, the Attou model has been utilized in the following work.

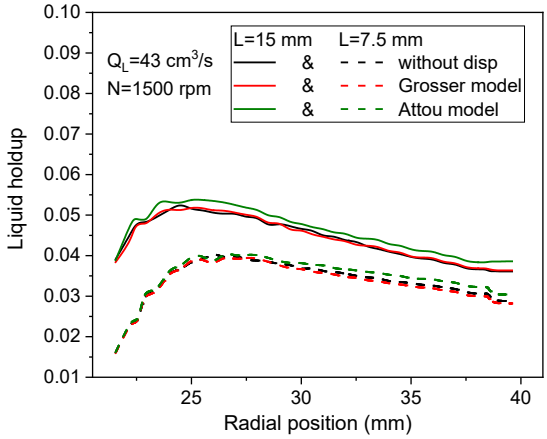

Figure 7. The effect of the capillary pressure models on the liquid holdup.

(ii) Spread factor in the dispersion force model

The spread factor, S_f, which is the only estimated parameter for the mechanical dispersion model, determines the magnitude of the drift velocity and thus influences the dispersion of the liquid. By conducting the tracer experiments of the CPBs, Hoek et al. (1986) investigated the effect of the packing particle size on the spread factor and proposed a correlation for the spread factor ($S_f = 0.12d_w$). In addition, the packing particle shape was considered, and the correlation ($S_f = 0.015d_w^{0.5}\phi^{-0.33}$) was suggested by Baldi and Specchia (1976). However, this does not take into account the liquid surface tension, thus, another correlation ($S_f = 0.231d_w^{0.5}\sigma$) was introduced (Onda et al., 1973), which is dependent of the particle size and surface tension.

Similar to the capillary pressure force, the mechanical dispersion force is also considered as a source term in the momentum equation. The effect of the different correlations discussed above for the spread factor on the liquid holdup along the radial direction of the RPB has been investigated as shown in Figure 8 where only the mechanical dispersion forces have been considered, without including the capillary

pressure force. When the nozzle length is 15 mm, the effect of the mechanical dispersion force on the liquid holdup is relatively small. The reason is that the liquid holdup in the packing region is relatively small in three flow directions due to the large nozzle length. This leads to a small spatial gradient of the liquid holdup and a small driving force to cause the liquid to flow from the high liquid fraction region to the low liquid fraction region and subsequently result in a small increase in the liquid holdup due to dispersion. It also can be observed that the red curve increases slightly with respect to the black curve because of the very small spread factor, which is 4.8×10^{-5}. For the nozzle length being 7.5 mm, the blue and olive curves, whose spread factors respectively are 3.0×10^{-4} and 3.3×10^{-4}, are clearly higher than the red curve. Therefore, it can be concluded that the spread factor is a very sensitive quantity for flows with a less uniform and more concentrated distribution, such as those for the case of the nozzle length being 7.5 mm.

It was reported that the correlations of Baldi and Specchia (1976) and Onda et al. (1973) was more consistent with the experimental data of CPBs (Lappalainen et al., 2009). In addition, the distributions of the liquid holdup in the packing region of the RPB are similar when employing the above two mechanical dispersion models as shown in Figure 8, which means that both models can be theoretically utilized in the RPB. Nevertheless, Baldi and Specchia (1976) studied the influence of the shape of the packing elements by using beads, Berl saddles and Raschig rings, but not the wire mesh used in this paper. In addition, the surface tension can affect the liquid dispersion (Delgado, 2005), and this factor is considered when the spread factor is estimated using $0.231 d_w^{0.5}\sigma$, thus this correlation has been selected in the work presented in the remainder of this paper.

So far, the suitable capillary pressure and mechanical dispersion models have been assessed. The significance of the capillary pressure force and mechanical dispersion force to the predicted liquid holdup can be assessed by comparing Figures 7 and 8. It is noted that the influences of the capillary pressure force and mechanical dispersion force

on the liquid hold up are in a similar order of magnitude for the case when the nozzle length is 15 mm. When for the nozzle length is 7.5 mm, the predicted liquid dispersion in this RPB is dominated by the mechanical dispersion and the capillary effect is small.

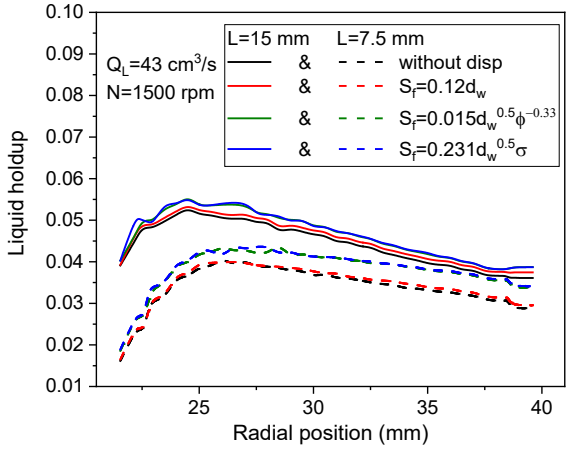

Figure 8. The effect of the correlations for the spread factor on the liquid holdup.

3.3 Effect of the operational parameters on the dispersion force

The effect of the operational parameters on the dispersion force has been investigated in the RPB models with the two liquid nozzle lengths of 15 and 7.5 mm. In addition, the effect of the dispersion forces on the liquid holdup with different operational parameters are similar for both the investigated liquid nozzle lengths. Therefore, in this section only the 7.5 mm nozzle length has been chosen to show the effect of the operational parameters on the dispersion force. In addition, in order to highlight the characteristics of the model when employing dispersion forces, the effect of the dispersion force on the liquid holdup have been analyzed by comparing the results of the liquid holdup predicted from the models with and without employing the dispersion forces.

3.3.1 The effect of liquid flow rate

Figure 9 illustrates the effect of the liquid flow rate on the liquid holdup in the packing region when the rotating speeds are 500 and 1000 rpm and the liquid flow rate varies from 23 to 43 cm^3/s. On taking the rotating speeds of 500 rpm as an example, Figures 10 and 11 show the predicted contour plots of the liquid holdup and the fractional effective interfacial area on the central/symmetric plane (z=0.01 m) without and with

considering the dispersion forces. It can be observed, when the liquid flow rate increases, more liquid exists in the packing region as shown in Figures 11(a) and 11(b), thus, the liquid volume fraction (holdup) becomes higher in the packing as can be seen in Figures 9(a) and 9(b). It also indicates that more of the packing surface is covered by the liquid phase. As a result, the effective interfacial area increases, and this is shown in Figures 11(c) and 11(d).

Compared with Figures 10 (a) and 11(a) or Figures 10(b) and 11(b), it is clear that the liquid distributes more uniformly under the influence of the liquid dispersion force. It further leads to a higher effective interfacial area, which is shown by comparing Figures 10(c) and 11(c) as well as Figures 10(d) and 11(d). Although it appears that the red area occupied in Figures 10(c) and 10(d) are larger than that in Figures 11(c) and 11(d), the fact is that the overall fractional effective interfacial area in Figures 11(c) and 11(d) increases. This is because the liquid is distributed more uniformly and more liquid covers the packing surface and is in contact with the gas phase due to the dispersion effect. Also, it can be seen from Figures 9(a) and 9(b) that the effect of the dispersion forces on the liquid holdup becomes larger with the increase in the liquid flow rate and this is due to the higher spatial gradient in the liquid holdup. However, the increase in the liquid holdup in Figure 9(b) is smaller when compared with that in Figure 9(a). The reason is that the liquid spreads into more tiny droplets due to the stronger interaction with packing and these droplets will obtain more kinetic energy when the rotational speed is higher. As a result, the dispersed liquid droplets achieve a larger radial velocity and they are difficult to retain in the packing region.

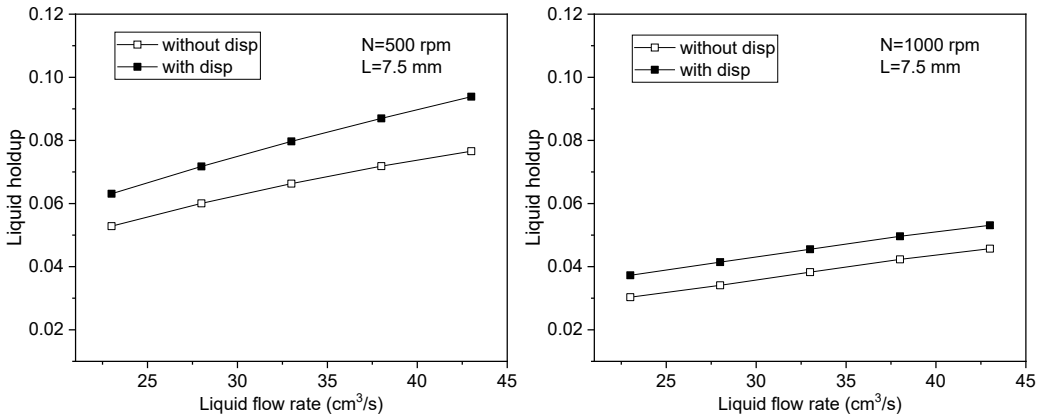

(a) (b)

Figure 9. The effect of the liquid flow rate on the liquid holdup under different rotational speeds: (a) 500 rpm and (b) 1000 rpm.

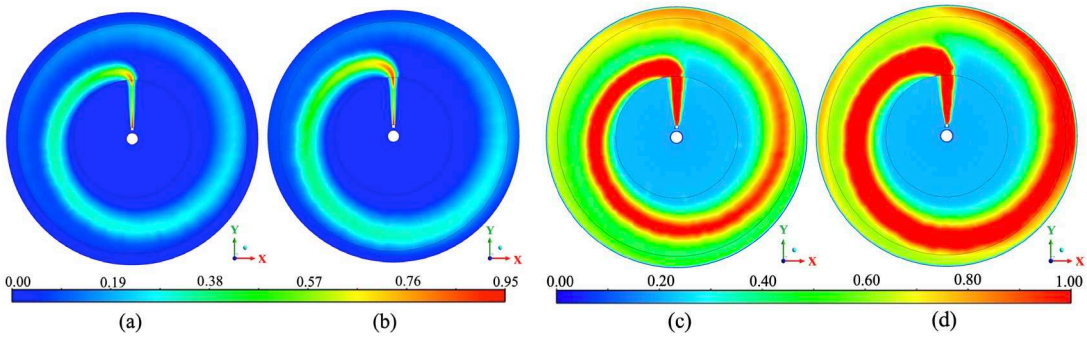

Figure 10. The holdup up and fractional effective interfacial area on the symmetric plane before employing the dispersion force with different liquid flow rates: (a) ε_L, 23 cm^3/s; (b) ε_L, 43 cm^3/s; (c) f_e, 23 cm^3/s; and (d) f_e, 43 cm^3/s.

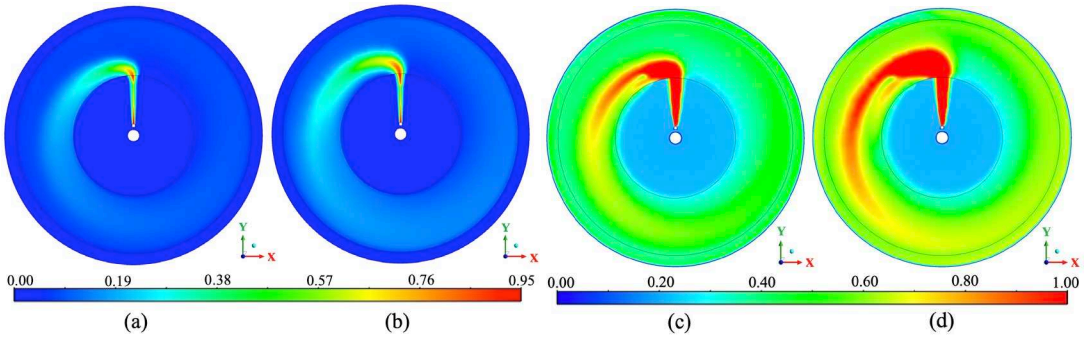

Figure 11. The holdup up and fractional effective interfacial area on the symmetric plane after employing the dispersion force with different liquid flow rates: (a) ε_L, 23 cm^3/s; (b) ε_L, 43 cm^3/s; (c) f_e, 23 cm^3/s; and (d) f_e, 43 cm^3/s.

3.3.2 Effect of the rotational speed and packing porosity

It has been proven that the rotational speed can influence the liquid flow dynamics and

liquid dispersion in the packing region (Liu et al., 2019; Wenzel and Górak, 2018a; Xie et al., 2017). Thus, the effect of the rotational speed on the liquid holdup is shown in Figure 12(a) when the liquid flow rate is 43 cm^3/s. When the rotational speed increases from 500 to 2500 rpm, the liquid can receive more kinetic energy from the rotating packing, and the liquid is formed into more tiny droplets and fragments, which can improve the liquid distribution and the effective interfacial area (Xie et al., 2017). Although the higher effective interfacial area can increase the liquid-solid drag force, the higher liquid radial velocity resulting from the stronger centrifugal force is predominant, thus leading to the liquid holdup reducing as shown in Figure 12(a). In addition, the lower liquid holdup and more uniform liquid distribution is caused by the higher rotational speed and this leads to a smaller spatial gradient of the liquid holdup, which causes the smaller liquid dispersion forces. Therefore, the increase in the magnitude of the liquid holdup reduces with the rotational speed increasing.

The packing porosity is an important characteristic for the RPBs and this factor may also affect the liquid holdup and liquid dispersion performance. Figure 12(b) shows the liquid holdup and liquid saturation with different porosity under the liquid flow rate of 23 cm^3/s. From Figure 12(b), it can be observed that the liquid saturation changes slightly and the liquid holdup decreases with the decreasing in the packing porosity. Reducing the packing porosity means that more wire mesh is stacked and occupied in the packing region, thus the fraction of the liquid volume (liquid holdup) would be smaller according to Eq. (2). In addition, the increase in the magnitude of the liquid holdup changes only slightly due to the almost unchanged liquid saturation and the spatial gradient of the liquid saturation.

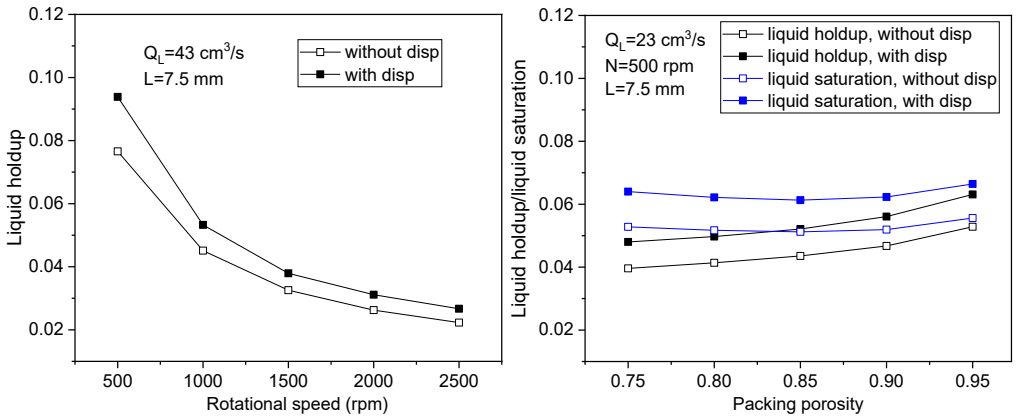

(a) (b)

Figure 12. The effect of the (a) rotational speed; and (b) packing porosity on the liquid holdup.

3.3.3 Effect of the nozzle size and number of nozzles

The nozzle size and the number of nozzles are very important for the initial liquid distribution and dispersion (Wu et al., 2020). Thus, Figures 13(a), 13(b) and 13(c) show the effect of the nozzle (axial) length, nozzle width, and number of nozzle(s) on the liquid holdup under the same liquid flow rate and rotational speed of 43cm^3/s and 500 rpm, respectively. In particular, the effect of the nozzle length on the liquid holdup has been rarely studied due to the limitation of the 2D model (Zhang et al., 2020). However, it can be studied by using the 3D model and its effect on the dispersion force has been investigated.

From Figure 13(a), with the increase in the nozzle length, the liquid jet velocity reduces and the liquid holdup distributes more uniformly in the packing region, especially in the axial direction (Yang et al., 2009). As a result, the liquid holdup in the packing region increases. In addition, as the nozzle length increases, the effect of the liquid dispersion force on the liquid holdup becomes weaker and this is due to two reasons. The first reason is the small spatial gradient in the liquid holdup in the packing region that results from the more uniform liquid distribution. The second is that the smaller liquid jet velocity leads to a smaller drift velocity, and the drift velocity is proportional to the mechanical dispersion force. However, the second reason is not the main reason,

and this is because the liquid jet velocity would substantially reduce after entering the packing so that it is only significant within a small entrance region although the initial impact on the packing and thus the dispersion is still important.

From Figure 13(b), the liquid holdup increases slightly with the increase in the nozzle width. The reason is that increasing the nozzle width not only reduces the liquid jet velocity, but also increases the liquid jet area in the horizontal direction, which could increase the liquid holdup. However, the flow in the packing is influenced more by the centrifugal force than the initial liquid jet velocity and jet area. Therefore, the increase of the liquid holdup is very limited. It is noted that this conclusion is contrast to that reported in the work of Zhang et al. (2020) where the liquid holdup increases significantly when the width of the nozzle increases. The possible reason is that Zhang et al. (2020) used a stationary packing and there is no centrifugal force generated when the liquid passes through the stationary wire mesh. In addition, the slight increase in the liquid holdup results in almost no change in the spatial gradient of the liquid holdup. Therefore, the nozzle width has little effect on the liquid dispersion performance.

It can be seen, from Figure 13(c), that the liquid holdup increases when the number of nozzles increases. When the liquid holdup increases from one to two and four, the liquid holdup increases from 5.3% to 8.0%, respectively. This indicates that the number of the nozzles has a larger influence on the liquid holdup when the nozzle number is small. Taking the symmetrical cross-sectional plane as an example, Figure 14 shows the distribution of the liquid holdup on this surface. It can be seen that the increasing number of nozzles could improve the liquid distribution in the radial and circumferential directions. The more uniform is the liquid distribution then this leads to a slightly lower spatial gradient of the liquid volume fraction. Therefore, the relative increase in the liquid holdup reduces slightly with the further increasing number of nozzles.

When compared with Figures 13(a)-13(c), it is noted that the liquid holdup is relatively sensitive to the nozzle length and number of nozzles rather than the nozzle width.

Therefore, employ a longer nozzle length can increase the liquid holdup, while, increasing the number of nozzles could lead to a more uniform liquid distribution, which may be good for the mass transfer performance.

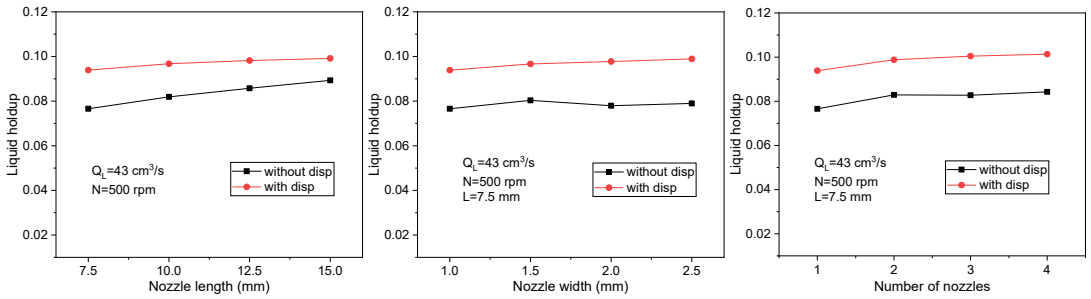

Figure 13. The effect of the (a) nozzle length; (b) nozzle width; and (c) number of nozzles, on the liquid holdup.

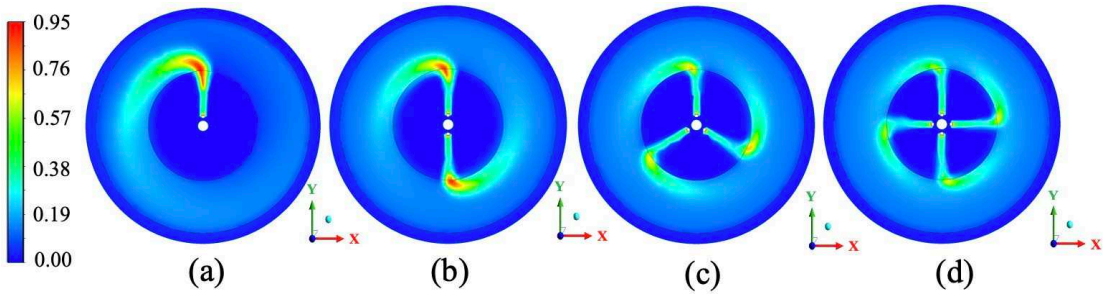

Figure 14. The distribution of the liquid holdup on the symmetric cross-sectional surface.

3.4 Comments on the time efficacy of the new Eulerian model

All the simulations presented in this paper have been performed using a PC with an Inter Core i7-7700k CPU and 8 processors. In general, it takes only 0.5-3 h depending on the rotational speed simulated to finish a full analysis of the 3D RPB. It should be noted that, in a 2D RPB model that is established based on the same experimental rig, a 0.87 M grid is chosen to investigate the flow characteristics when using the VOF method (Xie et al., 2017) compared with only about 0.05 M grid being required for the 3D simulation that has been performed in the present work. It is clear that a considerable amount of time and resource can be saved when using the Eulerian method without any

772 lose in accuracy.

773 **4. Conclusions**

774 The overall aim of this research is to develop an efficient and accurate modelling
775 approach that can be practically used for the modelling of the physical and chemical
776 processes occurring in a full scale rotational packed bed in the future. The specific
777 objectives of this paper are to investigate the liquid dispersion in the packing region,
778 and how to accurately model the effects in a RPB. In this study, a novel 3D Eulerian
779 porous medium RPB model has been developed and applied using the CFD software
780 package FLUENT, coupled with the interfacial, drag and dispersion forces. The
781 influence of the dispersion forces on the liquid holdup was investigated and the
782 sensitivity of the CFD predictions on the dispersion model employed, together with the
783 influence of the design and operational parameters such as the rotational speed, liquid
784 flow rate, etc. have been critically analyzed. Some of the main findings are as follows:
785 (i) the porous medium model with the Eulerian method was successfully developed
786 and used to model the fluid dynamics and liquid dispersion in a 3D RPB. Using this
787 model we can substantially reduce the computational time and efforts; (ii) a new form
788 of the porous resistance model was developed for two-phase flows and this model
789 could accurately predict the porous resistance in the packing (Bussière et al., 2017);
790 (iii) the correlation for the gas-liquid effective interfacial area was developed to fit the
791 non-uniform flow. After the modification, the distribution of the fractional effective
792 interfacial area (f_e) is consistent with the reality. The effective interfacial area is larger
793 where the liquid holdup is higher. In addition, the use of the developed f_e would make
794 the porous medium model more accurate; and (iv) the dispersion force models, for the
795 first time, were added into the model to simulate the liquid dispersion in a complete
796 packing region in 3D. In the 3D model coupled with the dispersion force models, the
797 effect of liquid dispersion on the liquid holdup could be quantified and more accurate
798 liquid flow performance was achieved.

799 The simulation results show that the effect of the capillary pressure and mechanical

dispersion forces on the liquid holdup are important to consider but showed different levels of significance with different liquid nozzle lengths. The effect of the capillary pressure force and mechanical dispersion force on the liquid holdup are similar when the nozzle length is 15 mm. While when the nozzle length is 7.5 mm, the liquid dispersion in this RPB model is dominated by the mechanical dispersion and the spread factor is a very sensitive quantity. With the liquid flow rate increasing, the influence of the dispersion force on the liquid holdup are slightly different under different rotational speeds. The effect of the dispersion force on the liquid holdup is almost the same with different nozzle widths and packing porosity. In addition, on increasing the number of the liquid nozzles from 1-4 could improve the liquid distribution and liquid holdup in the packing region substantially. However, further increasing the number of nozzles tends to be less effective. Certainly, establishing a universal model through thoroughly analyzing and combining the obtained results will be of much value for predicting the effect of the nozzles geometry and operating conditions on the liquid holdup. However, this idea is beyond the research scope of this paper and it is worthy of a full research paper in its own right. Therefore, this idea will be considered in the future work. Overall, the method proposed and employed in this paper paves the way for much more efficient simulations of full 3D RPBs in the future.

Acknowledgement

Support from the EPSRC UKCCSRC grant EP/P026214/1 is acknowledged.

References

Adamu, A., Russo-Abegão, F., Boodhoo, K., 2020. Process intensification technologies for CO_2 capture and conversion—a review. BMC Chem. Eng. 2, 1-18.

Attou, A., Boyer, C., Ferschneider, G., 1999. Modelling of the hydrodynamics of the cocurrent gas–liquid trickle flow through a trickle-bed reactor. Chem. Eng. Sci. 54, 785-802.

Attou, A., Ferschneider, G., 1999. A two-fluid model for flow regime transition in gas–

liquid trickle-bed reactors. Chem. Eng. Sci. 54, 5031-5037.

Baldi, G., Specchia, V., 1976. Distribution and radial spread of liquid in packed towers with two phase cocurrect flow: effect of packing shape and size. Quad. Ing. Chim. Ital. 12, 107-111.

Boyer, C., Koudil, A., Chen, P., Dudukovic, M.P., 2005. Study of liquid spreading from a point source in a trickle bed via gamma-ray tomography and CFD simulation. Chem. Eng. Sci. 60, 6279-6288.

Burns, J., Jamil, J., Ramshaw, C., 2000. Process intensification: operating characteristics of rotating packed beds—determination of liquid hold-up for a high-voidage structured packing. Chem. Eng. Sci. 55, 2401-2415.

Bussière, W., Rochette, D., Clain, S., André, P., Renard, J.B., 2017. Pressure drop measurements for woven metal mesh screens used in electrical safety switchgears. Int. J. Heat Fluid Flow 65, 60-72.

Carney, J.E., Finn, J.R., 2016. Device scale modeling of solvent absorption using MFIX-TFM. National Energy Technology Lab.(NETL), Albany, OR (United States).

Cortes Garcia, G.E., van der Schaaf, J., Kiss, A.A., 2017. A review on process intensification in HiGee distillation. J. Chem. Technol. Biot. 92, 1136-1156.

Delgado, J.M.P.Q., 2005. A critical review of dispersion in packed beds. Heat Mass Transfer. 42, 279-310.

Ergun, S., 1952. Fluid flow through packed columns. Chem. Eng. Prog. 48, 89-94.

Fourati, M., Roig, V., Raynal, L., 2013. Liquid dispersion in packed columns: experiments and numerical modeling. Chem. Eng. Sci. 100, 266-278.

Ghadyanlou, F., Azari, A., Vatani, A., 2021. A review of modeling rotating packed beds and improving their parameters: gas–liquid contact. Sustainability 13, 8046.

Grosser, K., Carbonell, R., Sundaresan, S., 1988. Onset of pulsing in two‐phase cocurrent downflow through a packed bed. AlChE J. 34, 1850-1860.

Gunjal, P.R., Kashid, M.N., Ranade, V.V., Chaudhari, R.V., 2005. Hydrodynamics of trickle-bed reactors: experiments and CFD modeling. Ind. Eng. Chem. Res. 44, 6278-

6294.
Guo, K., Zhang, Z., Luo, H., Dang, J., Qian, Z., 2014. An innovative approach of the effective mass transfer area in the rotating packed bed. Ind. Eng. Chem. Res. 53, 4052-4058.
Guo, T.Y., Cheng, K.P., Wen, L.X., Andersson, R., Chen, J.F., 2017. Three-dimensional simulation on liquid flow in a rotating packed bed reactor. Ind. Eng. Chem. Res. 56, 8169-8179.
Guo, T.Y., Shi, X., Chu, G.W., Xiang, Y., Wen, L.X., Chen, J.F., 2016. Computational fluid dynamics analysis of the micromixing efficiency in a rotating-packed-bed reactor. Ind. Eng. Chem. Res. 55, 4856-4866.
Hilpert, M., Repke, J.U., 2021. Experimental investigation and correlation of liquid-side mass transfer in pilot-scale rotating packed beds. Ind. Eng. Chem. Res. 60, 5251-5263.
Hoek, P., Wesselingh, J., Zuiderweg, F., 1986. Small scale and large scale liquid maldistribution in packed columns. Chem. Eng. Res. Des. 64, 431-449.
Iliuta, I., Larachi, F., Fourati, M., Raynal, L., Roig, V., 2014. Flooding limit in countercurrent gas–liquid structured packed beds—prediction from a linear stability analysis of an Eulerian two-fluid model. Chem. Eng. Sci. 120, 49-58.
Jiang, Y., Khadilkar, M., Al‐Dahhan, M., Dudukovic, M., 2002. CFD of multiphase flow in packed‐bed reactors: I. k‐Fluid modeling issues. AlChE J. 48, 701-715.
Kang, J.L., Sun, K., Wong, D.S.H., Jang, S.S., Tan, C.S., 2014. Modeling studies on absorption of CO_2 by monoethanolamine in rotating packed bed. Int. J. Greenh. Gas Con. 25, 141-150.
Kang, J.L., Wong, D.S.H., Jang, S.S., Tan, C.S., 2016. A comparison between packed beds and rotating packed beds for CO_2 capture using monoethanolamine and dilute aqueous ammonia solutions. Int. J. Greenh. Gas Con. 46, 228-239.
Kim, J., Pham, D.A., Lim, Y.I., 2016. Gas−liquid multiphase computational fluid dynamics (CFD) of amine absorption column with structured-packing for CO_2 capture.

884 Comput. Chem. Eng. 88, 39-49.
885 Kim, J., Pham, D.A., Lim, Y.I., 2017. Effect of gravity center position on amine
886 absorber with structured packing under offshore operation: computational fluid
887 dynamics approach. Chem. Eng. Res. Des. 121, 99-112.
888 Kołodziej, A., Łojewska, J., 2009. Experimental and modelling study on flow resistance
889 of wire gauzes. Chem. Eng. Process. 48, 816-822.
890 Kołodziej, A., Łojewska, J., Jaroszyński, M., Gancarczyk, A., Jodłowski, P., 2012. Heat
891 transfer and flow resistance for stacked wire gauzes: experiments and modelling. Int. J.
892 Heat Fluid Flow 33, 101-108.
893 Lappalainen, K., Alopaeus, V., Manninen, M., Aittamaa, J., 2008. Improved
894 hydrodynamic model for wetting efficiency, pressure drop, and liquid holdup in trickle-
895 bed reactors. Ind. Eng. Chem. Res. 47, 8436-8444.
896 Lappalainen, K., Manninen, M., Alopaeus, V., 2009. CFD modeling of radial spreading
897 of flow in trickle-bed reactors due to mechanical and capillary dispersion. Chem. Eng.
898 Sci. 64, 207-218.
899 Lappalainen, K., Gorshkova, E., Manninen, M., Alopaeus, V., 2011. Characteristics of
900 liquid and tracer dispersion in trickle-bed reactors: effect on CFD modeling and
901 experimental analyses. Comput. Chem. Eng. 35, 41-49.
902 Lateb, M., Masson, C., Stathopoulos, T., Bédard, C., 2013. Comparison of various types
903 of k–ε models for pollutant emissions around a two-building configuration. J. Wind
904 Eng. Ind. 115, 9-21.
905 Lee, J., Kolawole, T., Attidekou, P., 2017. Carbon capture from a simulated flue gas
906 using a rotating packed bed adsorber and mono ethanol amine (MEA). Energy Procedia
907 114, 1834–1840.
908 Liu, S., Long, J., 2000. Gas-liquid countercurrent flows through packed towers. J.
909 Porous Media 3.
910 Liu, W., Chu, G.W., Luo, Y., Liu, Y.Z., Meng, F.Y., Sun, B.C., Chen, J.F., 2019. Mass
911 transfer in a rotating packed bed reactor with a mesh-pin rotor: modeling and

912 experimental studies. Chem. Eng. J. 369, 600-610.
913 Liu, Y., Luo, Y., Chu, G.W., Larachi, F., Zou, H.K., Chen, J.F., 2020. Liquid microflow
914 inside the packing of a rotating packed bed reactor: computational, observational and
915 experimental studies. Chem. Eng. J. 386.
916 Liu, Y., Luo, Y., Chu, G.W., Luo, J.Z., Arowo, M., Chen, J.F., 2017. 3D numerical
917 simulation of a rotating packed bed with structured stainless steel wire mesh packing.
918 Chem. Eng. Sci. 170, 365-377.
919 Lu, X., Xie, P., Ingham, D.B., Ma, L., Pourkashanian, M., 2018. A porous media model
920 for CFD simulations of gas-liquid two-phase flow in rotating packed beds. Chem. Eng.
921 Sci. 189, 123-134.
922 Lu, X., Xie, P., Ingham, D.B., Ma, L., Pourkashanian, M., 2019a. Modelling of CO_2
923 absorption in a rotating packed bed using an Eulerian porous media approach. Chem.
924 Eng. Sci. 199, 302-318.
925 Lu, Y.Z., Liu, W., Xu, Y.C., Luo, Y., Chu, G.W., Chen, J.F., 2019b. Initial liquid
926 dispersion and mass transfer performance in a rotating packed bed. Chem. Eng. Process.
927 140, 136-141.
928 Luo, Y., Chu, G.W., Zou, H.K., Wang, F., Xiang, Y., Shao, L., Chen, J.F., 2012a. Mass
929 transfer studies in a rotating packed bed with novel rotors: chemisorption of CO_2. Ind.
930 Eng. Chem. Res. 51, 9164-9172.
931 Luo, Y., Chu, G.W., Zou, H.K., Zhao, Z.Q., Dudukovic, M.P., Chen, J.F., 2012b. Gas–
932 liquid effective interfacial area in a rotating packed bed. Ind. Eng. Chem. Res. 51,
933 16320-16325.
934 Luo, Y., Luo, J.Z., Chu, G.W., Zhao, Z.Q., Arowo, M., Chen, J.F., 2017. Investigation
935 of effective interfacial area in a rotating packed bed with structured stainless steel wire
936 mesh packing. Chem. Eng. Sci. 170, 347-354.
937 Ma, C., Su, M.J., Luo, Y., Chu, G.W., Sun, B.C., Chen, J.F., 2019. Wetting behavior of
938 the stainless steel wire mesh with Al_2O_3 coatings and mass transfer intensification in a
939 rotating packed bed. Ind. Eng. Chem. Res. 59, 1374-1382.

940 Mewes, D., Loser, T., Millies, M., 1999. Modelling of two-phase flow in packings and
941 monoliths. Chem. Eng. Sci. 54, 4729-4747.
942 Onda, K., Takeuchi, H., Maeda, Y., Takeuchi, N., 1973. Liquid distribution in a packed
943 column. Chem. Eng. Sci. 28, 1677-1683.
944 Ouyang, Y., Tang, K.L., Xiang, Y., Zou, H.K., Chu, G.W., Agarwal, R.K., Chen, J.F.,
945 2019. Evaluation of various turbulence models for numerical simulation of a multiphase
946 system in a rotating packed bed. Comput. Fluids 194.
947 Ouyang, Y., Wang, S., Xiang, Y., Zhao, Z., Wang, J., Shao, L., 2018a. CFD analyses of
948 liquid flow characteristics in a rotor-stator reactor. Chem. Eng. Res. Des. 134, 186-197.
949 Ouyang, Y., Xiang, Y., Gao, X.Y., Li, W.L., Zou, H.K., Chu, G.W., Chen, J.F., 2018b.
950 Micromixing efficiency in a rotating packed bed with non-Newtonian fluid. Chem. Eng.
951 J. 354, 162-171.
952 Ouyang, Y., Zou, H.K., Gao, X.Y., Chu, G.W., Xiang, Y., Chen, J.F., 2018c.
953 Computational fluid dynamics modeling of viscous liquid flow characteristics and end
954 effect in rotating packed bed. Chem. Eng. Process. 123, 185-194.
955 Pham, D.A., Lim, Y.I., Jee, H., Ahn, E., Jung, Y., 2015a. Effect of ship tilting and motion
956 on amine absorber with structured-packing for CO_2 removal from natural gas. AlChE
957 J. 61, 4412-4425.
958 Pham, D.A., Lim, Y.I., Jee, H., Ahn, E., Jung, Y., 2015b. Porous media Eulerian
959 computational fluid dynamics (CFD) model of amine absorber with structured-packing
960 for CO_2 removal. Chem. Eng. Sci. 132, 259-270.
961 Shi, X., Xiang, Y., Wen, L.X., Chen, J.F., 2013. CFD analysis of liquid phase flow in a
962 rotating packed bed reactor. Chem. Eng. J. 228, 1040-1049.
963 Shih, T.H., Liou, W.W., Shabbir, A., Yang, Z., Zhu, J., 1995. A new k–ε eddy viscosity
964 model for high Reynolds number turbulent flows. Comput. Fluids 24, 227-238.
965 Solomenko, Z., Haroun, Y., Fourati, M., Larachi, F., Boyer, C., Augier, F., 2015. Liquid
966 spreading in trickle-bed reactors: experiments and numerical simulations using
967 Eulerian–Eulerian two-fluid approach. Chem. Eng. Sci. 126, 698-710.

968 Su, M.J., Luo, Y., Chu, G.W., Cai, Y., Le, Y., Zhang, L.L., Chen, J.F., 2020. Dispersion
969 behaviors of droplet impacting on wire mesh and process intensification by surface
970 micro/nano-structure. Chem. Eng. Sci. 219, 115593.
971 Wang, J.Q., Ouyang, Y., Li, W.L., Esmaeili, A., Xiang, Y., Chen, J.F., 2020. CFD
972 analysis of gas flow characteristics in a rotating packed bed with randomly arranged
973 spherical packing. Chem. Eng. J. 385.
974 Wang, Y., Chen, J., Larachi, F., 2013. Modelling and simulation of trickle‐bed reactors
975 using computational fluid dynamics: a state‐of‐the‐art review. Can. J. Chem. Eng.
976 91, 136-180.
977 Wang, Y., Li, Y.B., Su, M.J., Chu, G.W., Sun, B.C., Luo, Y., 2021. Liquid droplet
978 dispersion in a rotating packed bed: experimental and numerical studies. Chem. Eng.
979 Sci. 240.
980 Wang, Z., Yang, T., Liu, Z., Wang, S., Gao, Y., Wu, M., 2019. Mass transfer in a rotating
981 packed bed: a critical review. Chem. Eng. Process. 139, 78-94.
982 Wenzel, D., Gerdes, N., Steinbrink, M., Ojeda, L.S., Górak, A., 2018a. Liquid
983 distribution and mixing in rotating packed beds. Ind. Eng. Chem. Res. 58, 5919-5928.
984 Wenzel, D., Górak, A., 2018b. Review and analysis of micromixing in rotating packed
985 beds. Chem. Eng. J. 345, 492-506.
986 Wu, W., Luo, Y., Chu, G.W., Liu, Y., Zou, H.K., Chen, J.F., 2018. Gas flow in a
987 multiliquid-inlet rotating packed bed: three-dimensional numerical simulation and
988 internal optimization. Ind. Eng. Chem. Res. 57, 2031-2040.
989 Wu, W., Luo, Y., Chu, G.W., Su, M.J., Cai, Y., Zou, H.K., Chen, J.F., 2020. Liquid flow
990 behavior in a multiliquid-inlet rotating packed bed reactor with three-dimensional
991 printed packing. Chem. Eng. J. 386, 121537.
992 Xie, P., Lu, X., Ding, H., Yang, X., Ingham, D., Ma, L., Pourkashanian, M., 2019. A
993 mesoscale 3D CFD analysis of the liquid flow in a rotating packed bed. Chem. Eng.
994 Sci. 199, 528-545.
995 Xie, P., Lu, X., Yang, X., Ingham, D., Ma, L., Pourkashanian, M., 2017. Characteristics

of liquid flow in a rotating packed bed for CO_2 capture: a CFD analysis. Chem. Eng. Sci. 172, 216-229.

Xu, Y.C., Li, Y.B., Liu, Y.Z., Luo, Y., Chu, G.W., Zhang, L.L., Chen, J.F., 2019. Liquid jet impaction on the single‐layer stainless steel wire mesh in a rotating packed bed reactor. AlChE J. 65.

Yang, K., Chu, G., Zou, H., Sun, B., Shao, L., Chen, J.F., 2011. Determination of the effective interfacial area in rotating packed bed. Chem. Eng. J. 168, 1377-1382.

Yang, K., Chu, G.W., Shao, L., Luo, Y., Chen, J.F., 2009. Micromixing efficiency of rotating packed bed with premixed liquid distributor. Chem. Eng. J. 153, 222-226.

Yang, W., Wang, Y., Chen, J., Fei, W., 2010. Computational fluid dynamic simulation of fluid flow in a rotating packed bed. Chem. Eng. J. 156, 582-587.

Yang, Y., Xiang, Y., Chu, G., Zou, H., Luo, Y., Arowo, M., Chen, J.F., 2015a. A noninvasive X-ray technique for determination of liquid holdup in a rotating packed bed. Chem. Eng. Sci. 138, 244-255.

Yang, Y., Xiang, Y., Chu, G., Zou, H., Sun, B., Arowo, M., Chen, J.F., 2016. CFD modeling of gas–liquid mass transfer process in a rotating packed bed. Chem. Eng. J. 294, 111-121.

Yang, Y., Xiang, Y., Li, Y., Chu, G., Zou, H., Arowo, M., Chen, J., 2015b. 3D CFD modelling and optimization of single-phase flow in rotating packed beds. Can. J. Chem. Eng. 93, 1138-1148.

Yang, Y.C., Ouyang, Y., Zhang, N., Yu, Q.J., Arowo, M., 2019. A review on computational fluid dynamic simulation for rotating packed beds. J. Chem. Technol. Biot. 94, 1017-1031.

Yi, F., Zou, H.K., Chu, G.W., Shao, L., Chen, J.F., 2009. Modeling and experimental studies on absorption of CO_2 by Benfield solution in rotating packed bed. Chem. Eng. J. 145, 377-384.

Zhang, C., Bokil, A., 1997. A quasi-three-dimensional approach to simulate the two-phase fluid flow and heat transfer in condensers. Int. J. Heat Mass Transfer 40, 3537-

3546.

Zhang, J.P., Luo, Y., Chu, G.W., Sang, L., Liu, Y., Zhang, L.L., Chen, J.F., 2017. A hydrophobic wire mesh for better liquid dispersion in air. Chem. Eng. Sci. 170, 204-212.

Zhang, W., Xie, P., Li, Y., Teng, L., Zhu, J., 2020. CFD analysis of the hydrodynamic characteristics in a rotating packed bed with multi-nozzles. Chem. Eng. Process. 158.

Zheng, X.H., Chu, G.W., Kong, D.J., Luo, Y., Zhang, J.P., Zou, H.K., Zhang, L.L., Chen, J.F., 2016. Mass transfer intensification in a rotating packed bed with surface-modified nickel foam packing. Chem. Eng. J. 285, 236-242.